Optics Letters

Simple differential digital confocal aperture to improve axial response of line-scanning confocal microendoscopes

Yubo Tang,[1,*] Alex Kortum,[1] Imran Vohra,[1] Jennifer Carns,[1] Sharmila Anandasabapathy,[2] and Rebecca Richards-Kortum[1]

[1]Bioengineering, Rice University, Houston, Texas 77005, USA
[2]Baylor College of Medicine, Houston, Texas 77030, USA
*Corresponding author: yt9@rice.edu

Received 2 May 2019; revised 22 July 2019; accepted 13 August 2019; posted 14 August 2019 (Doc. ID 366564); published 10 September 2019

Line-scanning confocal microendoscopy offers video-rate cellular imaging of scattering tissue with relatively simple hardware, but its axial response is inferior to that of point-scanning systems. Based on Fourier optics theory, we designed differential confocal apertures with a simple subtraction technique to improve the line-scanning sectioning performance. Taking advantage of digital slit apertures on a digital light projector and a CMOS rolling shutter, we demonstrate real-time optical sectioning performance comparable to point scanning in a dual-camera microendoscope (<$6,000). We validate the background rejection capability when imaging porcine columnar epithelium stained with fluorescent contrast agents with different uptake mechanisms and staining properties.

https://doi.org/10.1364/OL.44.004519

Probe-based fluorescence microendoscopy has demonstrated great potential to improve early cancer detection. When imaging thick, highly scattering biological tissue, the high level of scattering usually necessitates suppressing unwanted out-of-focus signal to obtain images with good contrast. To achieve this goal, different strategies have been employed. On the sample end of the probe, contrast agents that predominantly accumulate in specific cellular components or target specific biomarkers have been used. Proflavine, for example, is a topical contrast agent that preferentially stains the nuclei and has been clinically validated [1–4]. On the proximal end of the probe, optical sectioning can be employed to selectively collect fluorescence from the in-focus plane [5,6].

Line-scanning confocal imaging is an appealing technique for clinical translation, since it allows for video-speed frame rate at relatively low complexity and cost. Compared with point scanning, however, the axial sectioning performance is inferior. Specifically, line scanning has a poorer full width at half maximum (FWHM). Moreover, it suffers from slow attenuation of out-of-focus signal over a long axial range [7]. Subtraction techniques have been reported to improve the line-scanning axial response, but these methods either require multiple frames or suffer from undesired artifacts [6,8]. Previously, we demonstrated a line-scanning confocal high-resolution microendoscope (LSC HRME) using digital apertures on a digital light projector (DLP) and a CMOS rolling shutter [9]. In this Letter, we leverage the digitally programmed apertures to further improve the axial performance with a simple real-time subtraction technique. Using simulated and experimental data, we demonstrate differential aperture confocal (DAC) imaging in a low-cost dual-camera microendoscope that has improved axial response in both near and far defocus ranges (0–100 μm and >100 μm defocus in this study, respectively). We further validate the system performance by imaging highly scattering porcine columnar epithelium with proflavine staining. We also explore the ability of the system to image non-specific topical fluorescein staining, which has recently been shown to be useful for columnar crypt characterization but shows a higher level of scattered background [10].

DAC HRME is a dual-camera line-scanning fluorescence microscope, shown in Fig. 1(a). Blue light from a LightCrafter 4500 DLP (Texas Instruments; total power is 1.3 mW at the sample end in each confocal scanning cycle) is collimated by a lens ($f = 125$ mm) that replaces the built-in DLP lens to provide fluorescence excitation. Two 8-bit CMOS sensors (Mako U503, Allied Vision) were used for fluorescence descanning in rolling shutter mode. The microscope is coupled with a coherent fiber bundle [FIGH-30-850N, Myriad Fiber Imaging; 790 μm circular field of view (FOV)] as an image relay, and collected fluorescence is divided by a beam splitter.

The spatiotemporal aperture alignment for confocal imaging is illustrated in Fig. 1(b). Detailed scanning characteristics of the DLP and CMOS rolling shutter have been described elsewhere [9]. Briefly, the DLP binary illumination sequence (blue rectangles) is projected discretely due to the need to toggle micromirrors, and the CMOS rolling shutter (green parallelogram) scans in a synchronized manner. We implement parallel illumination to improve the axial response by reducing the aperture width. In the dual-camera setup, CMOS 1 is used to capture the LSC images, using illumination and standard

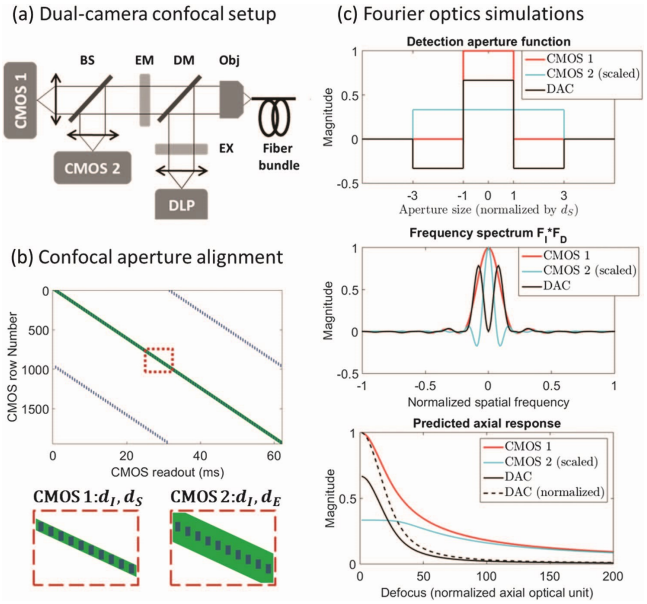

Fig. 1. (a) DAC HRME setup, (b) confocal aperture alignment, and (c) simulations of different imaging configurations based on Fourier optics. In (c), the confocal apertures together with the resulting frequency spectra and axial responses are plotted for CMOS 1, CMOS 2, and differential aperture confocal imaging; simulated values are normalized by the maxima in the CMOS 1 configuration, unless otherwise noted. EM, emission filter (500 nm long pass); EX, excitation filter (452/45 nm bandpass); DM, dichroic mirror (490 nm long pass); BS, beam splitter; Obj, objective.

detection aperture widths of d_I and d_S. On CMOS 2, we capture a second frame within the same DLP scan but use an expanded detection aperture d_E for DAC subtraction in real time.

The axial response of confocal scanning can be modeled in the context of Fourier optics theory [11,12]. In the frequency domain, the axial profile of a confocal system is

$$I(\mu) = N_0 \iint F_I(m,n)F_D(m,n)C^2(m,n;\mu)\mathrm{d}m\mathrm{d}n, \quad (1)$$

in which N_0 is a normalizing constant, m and n are normalized spatial frequencies in the x and y directions, and μ is the defocus in the normalized axial optical unit; $F_I(m,n)$ and $F_D(m,n)$ represent frequency spectra, or Fourier transforms of confocal illumination and detection apertures, respectively; $C(m,n;\mu)$ describes the optical transfer function [13]. Equation (1) shows that the confocal axial response is an integral of optical sectioning strength of all spatial frequencies through the imaging system, and their relative contribution is modulated by the frequency spectra of confocal apertures. It also reveals that optical sectioning at defocus μ is exhibited only in the optical transfer function $C(m,n;\mu)$, which can be calculated with Stokseth's approximation:

$$g(\mu,\delta) = \begin{cases} \Gamma(\delta)\cdot\left\{2\frac{J_1\left[\mu\delta\left(1-\frac{\delta}{2}\right)\right]}{\mu\delta\left(1-\frac{\delta}{2}\right)}\right\}, & \text{if } 0<\delta<2, \\ 0, \quad if 2\le\delta \end{cases}$$

$$\Gamma(\delta) = 1 - 0.69\delta + 0.0076\delta^2 + 0.0437\delta^3, \quad (2)$$

where $\delta = \sqrt{m^2+n^2}$, and J_1 denotes the first-order Bessel function of the first kind [14].

We first consider LSC imaging on CMOS 1 in Fig. 1(c). The confocal apertures along the x axis are

$$A_I = \mathrm{rect}\left(\frac{x}{d_I}\right), \qquad A_D^S = \mathrm{rect}\left(\frac{x}{d_S}\right), \quad (3)$$

with A_I and A_D^S denoting the illumination aperture and the detection aperture of a standard width [Fig. 1(c), top]. The corresponding frequency spectrum $F_I(m,n) * F_D(m,n)$ is a bandpass filter centered at zero [Fig. 1(c), middle]. The LSC axial response using a standard detection aperture can be calculated as

$$I_S(\mu) = Npq_S \cdot \int \mathrm{sinc}\left(\frac{pm}{2\pi}\right)\mathrm{sinc}\left(\frac{q_S m}{2\pi}\right)g^2(\mu,m)\mathrm{d}m, \quad (4)$$

in which N is a normalizing constant, p and q_S are aperture widths d_I and d_S measured in normalized lateral optical units [8]. As revealed by Eq. (2), the zero to low frequencies at the center of the LSC spectrum are the slowly attenuating components along the axial axis. This contributes to the residual background far from the focus shown in the predicted axial response of LSC imaging on CMOS 1.

Importantly, Eqs. (1), (2), and (4) also indicate that the frequency spectrum can be employed to tune the confocal sectioning performance. In order to further suppress the zero to low frequencies in the LSC configuration, we program an expanded detection aperture of a physical width d_E (q_E in the normalized optical unit) on CMOS 2 and engineer a virtual detection aperture with a simple subtraction:

$$A_D^{\mathrm{DAC}} = A_D^S - \frac{d_S}{d_E}A_D^E = \mathrm{rect}\left(\frac{x}{d_S}\right) - \frac{d_S}{d_E}\mathrm{rect}\left(\frac{x}{d_E}\right). \quad (5)$$

In other words, a scaled image from CMOS 2 with an expanded detection aperture A_D^E is used to selectively collect the poorly attenuating frequency components:

$$I_E(\mu) = Npq_E \cdot \int \mathrm{sinc}\left(\frac{pm}{2\pi}\right)\mathrm{sinc}\left(\frac{q_E m}{2\pi}\right)g^2(\mu,m)\mathrm{d}m, \quad (6)$$

which can then be subtracted from the LSC image on CMOS 1. The resulting DAC frequency spectrum in Fig. 1(c) (middle) reveals a bimodal distribution that excludes the zero frequency and suppresses low frequencies (in this example, $q_E = 3q_S$). The corresponding axial response for DAC imaging is

$$\begin{aligned} I_{\mathrm{DAC}}(\mu) &= I_S(\mu) - \frac{q_S}{q_E}I_E(\mu) \\ &= Npq_S \cdot \int \mathrm{sinc}\left(\frac{pm}{2\pi}\right)\left[\mathrm{sinc}\left(\frac{q_S m}{2\pi}\right)\right. \\ &\quad \left. - \mathrm{sinc}\left(\frac{q_E m}{2\pi}\right)\right]g^2(\mu,m)\mathrm{d}m. \end{aligned} \quad (7)$$

As expected, the simulated DAC axial response in Fig. 1(c) (bottom) shows further attenuation of out-of-focus signal, especially in the far defocus range.

Like other subtraction-based techniques such as structured illumination demodulation, there exists a tradeoff between background subtraction and signal loss when determining the q_E/q_S ratio. Theoretically, a wider q_E can reject the zero frequency more exclusively but is less effective in suppression of low frequencies. In addition, since the aperture width is directly

proportional to the exposure time, it is not practical to use high q_E/q_S ratios beyond the camera's dynamic range. Based on our experimental data, we used a q_E/q_S ratio of 3; a 70:30 beam splitter was selected accordingly to effectively leverage the dynamic range of both cameras.

We experimentally characterized the axial response by imaging a mirror in reflection mode without the emission filter or the fiber bundle in Fig. 2(a). As anticipated, background signals far from the focus were observed on both cameras and they converged from about 150 μm, confirming that similar underlying zero and low frequencies were captured. After the subtraction, the FWHM was improved, and background far from the focus was eliminated. We calculated the optical sectioning performance using Eqs. (2), (4), (6), and (7) and parameters from our experimental setup (d_S and d_E on two cameras were 22.6 μm and 67.7 μm on the object plane). The FWHM from the theoretical simulations was 114.2 μm in the LSC configuration and reduced to 75.1 μm in the DAC configuration. In addition, we modeled the point-scanning axial response using pinhole diameters that were the same as the LSC slit widths, showing a simulated FWHM of 61.5 μm with rapid attenuation with defocus. These results suggest that the DAC axial response was superior to the LSC and was comparable to a point-scanning setup, especially in the far defocus range.

The findings above were further validated in fluorescence mode by imaging a single layer of 15 μm beads (F-21010, Thermo Fisher Scientific) with the fiber bundle. In Fig. 2(b), images in focus, at 40 μm and 80 μm defocus are shown.

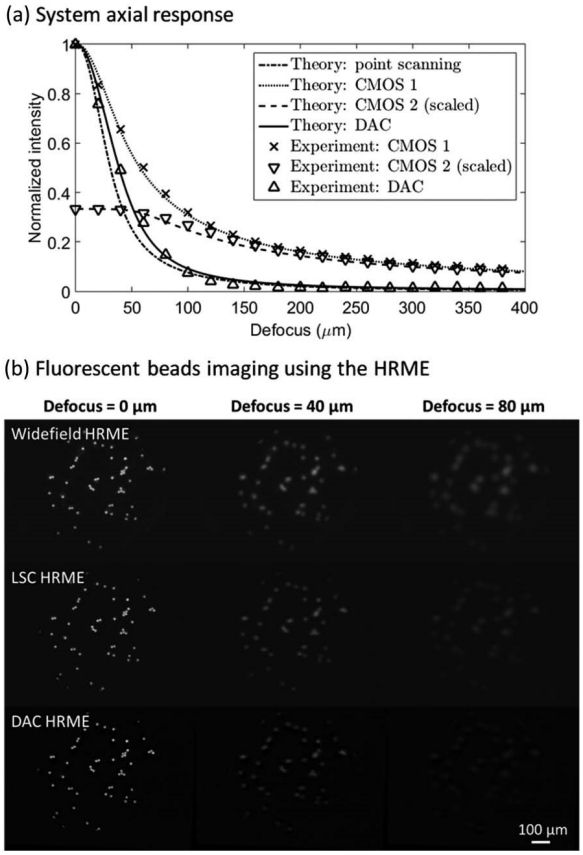

Fig. 2. (a) Axial responses of different imaging configurations (theory and experiment), and (b) fluorescent beads imaging using the HRME.

To facilitate visualization, the in-focus widefield image was normalized to itself, and widefield images at other defocus values were equally boosted to ensure that the relative intensities of all widefield images remained the same after adjustment; the same procedure was performed for LSC and DAC HRME images. The non-scanning widefield HRME images revealed defocus blur but minimal signal loss. At 40 μm, the DAC HRME images demonstrated better signal rejection. At 80 μm, residual signal observed in the LSC HRME image was significantly attenuated with the DAC HRME.

The enhanced out-of-focus background rejection with the DAC HRME is further evaluated by imaging excised porcine stomach tissue. The gastric mucosa is characterized by a superficial lining of columnar cells, invaginations called gastric pits, and gastric glands that form at the pit base and grow towards the surface. Given the high cellular density, optical sectioning is desired to examine this unique architecture. During *ex vivo* imaging, fresh porcine stomach tissue was acquired from a local abattoir and imaged within two hours after resection. The mucosa was topically stained with either proflavine (0.01% w/v in PBS) or fluorescein (0.05% w/v in PBS) and rinsed with PBS prior to imaging.

Proflavine-stained gastric mucosa images are shown in Fig. 3, highlighting nuclear staining on the surface epithelial lining and glands within the pits. The LSC image better resolved the surface mucosa and the transitional lining into the pits than the widefield image. In the DAC image, the contrast of individual nuclei (white arrows) on the superficial surface was further enhanced. Importantly, while residual background within the gastric pits was still present in the LSC image, it was significantly reduced in the DAC image. This allowed for clearer visualization of the glandular structures and could be

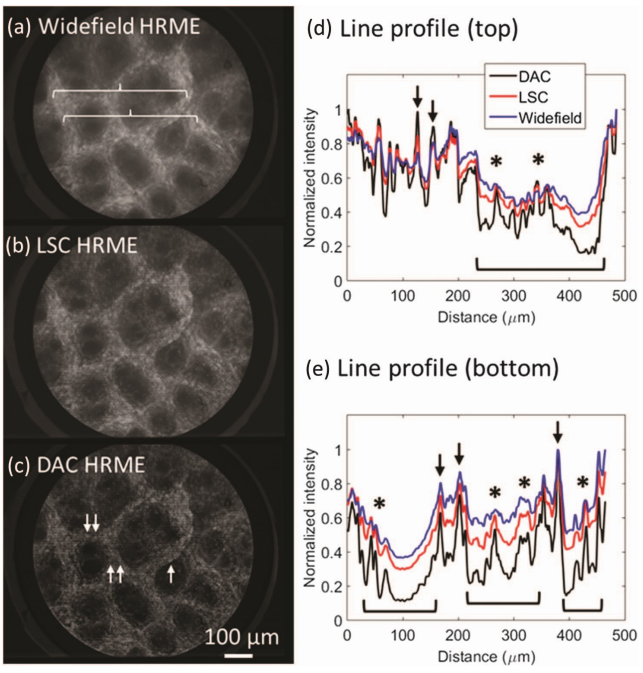

Fig. 3. *Ex vivo* imaging of gastric columnar epithelium stained with proflavine. Two lines indicated by braces in (a) are profiled in (d) and (e), highlighting enhanced contrast of nuclei (arrows) on the superficial lining and glandular structures (asterisks) within the pits (brackets) in the DAC image.

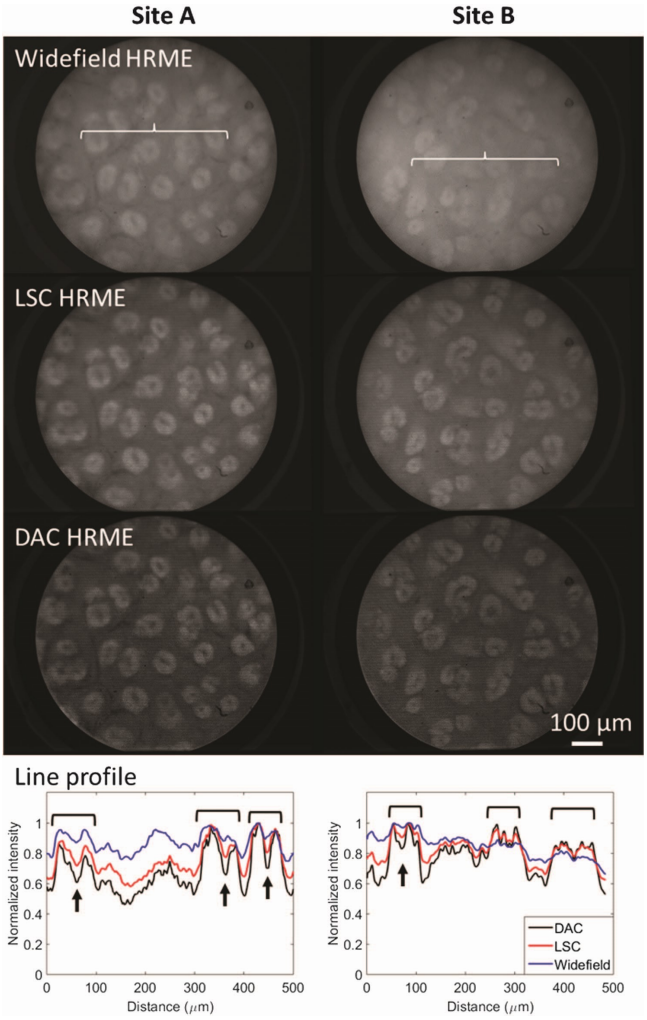

Fig. 4. *Ex vivo* imaging of gastric columnar epithelium stained with fluorescein. Two lines indicated by the braces in the widefield images are quantified, showing enhanced contrast of pits (brackets) and lower signal levels due to elevated glands (arrows).

attributed to improved rejection of scattered signal from depths greater than 100 μm. These findings were confirmed in two line [braces in Fig. 3(a)] profiles in Figs. 3(d) and 3(e), showing improved contrast of individual nuclei on the surface lining (black arrows) and glandular structures within the pits [asterisks within the brackets in Fig. 3(e)].

Images with topical fluorescein staining are shown in Fig. 4. Non-specific fluorescein filled the pits and showed a complementary pattern. Not surprisingly, the greater level of background signal from fluorescein-stained tissue resulted in poor contrast in widefield images. With confocal scanning, the cobblestone architecture could be readily discerned, with the contrast enhancement most striking in the DAC images. In addition, lower signal levels were seen at the center, which could be due to the elevation of glands within the pit. The differences were quantified in two line profiles (white braces in the widefield images), with the DAC images revealing sharp transition across the pits and the surface lining. Notably, due to its capability to reject long-range background, the DAC images better highlighted the glandular elevation that appeared dark (black arrows in line profiles) within the pits.

In summary, we present DAC imaging to improve the axial response of confocal line scanning based on Fourier optics, and we implement a simple subtraction technique using digital apertures on a DLP and two CMOS sensors. Our *ex vivo* imaging results demonstrate its potential for high-resolution imaging in clinically important yet challenging applications, including imaging highly scattering columnar epithelium with both specific and non-specific contrast agents. The versatile digital aperture framework provides a convenient way to implement optical sectioning in non-confocal microscopes, and the synthetic aperture approach can also be readily adopted to improve axial performance of existing line-scanning confocal microscopes, including these with physical scanners and apertures.

Funding. Dan L. Duncan Cancer Center, Baylor College of Medicine (DLDCC); National Cancer Institute (NCI) (R01CA103830); National Science Foundation (NSF) (1730574).

Acknowledgment. The authors thank Drs. Richard Schwarz and Sadhna Dhingra for helpful discussions.

REFERENCES

1. M. C. Pierce, P. M. Vila, A. D. Polydorides, R. Richards-Kortum, and S. Anandasabapathy, Am. J. Gastroenterol. **106**, 1722 (2011).
2. B. Hunt, J. H. T. Fregnani, R. A. Schwarz, N. Pantano, S. Tesoni, J. C. Possati-Resende, M. Antoniazzi, B. de Oliveira Fonseca, G. de Macedo Matsushita, C. Scapulatempo-Neto, L. Kerr, P. E. Castle, K. Schmeler, and R. Richards-Kortum, Cancer Prev. Res. **11**, 359 (2018).
3. Y. Tang, A. D. Polydorides, S. Anandasabapathy, and R. R. Richards-Kortum, J. Biomed. Opt. **23**, 1 (2018).
4. T. Quang, R. A. Schwarz, S. M. Dawsey, M. C. Tan, K. Patel, X. Yu, G. Wang, F. Zhang, H. Xu, S. Anandasabapathy, and R. Richards-Kortum, Gastrointest. Endosc. **84**, 834 (2016).
5. P. Keahey, P. Ramalingam, K. Schmeler, and R. R. Richards-Kortum, Proc. Natl. Acad. Sci. USA **113**, 10769 (2016).
6. M. Hughes and G. Yang, Biomed. Opt. Express **7**, 2257 (2016).
7. Y. G. Patel, M. Rajadhyaksha, and C. A. DiMarzio, Biomed. Opt. Express **2**, 2231 (2011).
8. V. Poher, G. T. Kennedy, H. B. Manning, D. M. Owen, H. X. Zhang, E. Gu, M. D. Dawson, P. M. W. French, and M. A. A. Neil, Opt. Lett. **33**, 1813 (2008).
9. Y. Tang, A. Kortum, I. Vohra, M. Othman, S. Dhingra, N. Mansour, J. Carns, S. Anandasabapathy, and R. Richards-Kortum, Opt. Lett. **44**, 654 (2019).
10. S. P. Prieto, K. K. Lai, J. A. Laryea, J. S. Mizell, W. C. Mustain, and T. J. Muldoon, Biomed. Opt. Express **8**, 2324 (2017).
11. T. Wilson and S. J. Hewlett, J. Microsc. **160**, 115 (1990).
12. C. J. R. Sheppard and X. Q. Mao, J. Mod. Opt. **35**, 1169 (1988).
13. T. Wilson, J. Microsc. **242**, 111 (2011).
14. P. A. Stokseth, J. Opt. Soc. Am. **59**, 1314 (1969).